A study of the radiation tolerance of poly-crystalline and single-crystalline CVD diamond to 800 MeV and 24 GeV protons

L Bäni[24,30], A Alexopoulos[3], M Artuso[20], F Bachmair[24], M Bartosik[3],
H Beck[23], V Bellini[2], V Belyaev[12], B Bentele[19], A Bes[27], J-M Brom[7],
M Bruzzi[4], G Chiodini[26], D Chren[18], V Cindro[9], G Claus[7], J Collot[27],
J Cumalat[19], A Dabrowski[3], R D'Alessandro[4], D Dauvergne[27], W de Boer[10],
S Dick[13], C Dorfer[24], M Dünser[3], V Eremin[6], G Forcolin[22], J Forneris[15],
L Gallin-Martel[27], M-L Gallin-Martel[27], K K Gan[13], M Gastal[3], C Giroletti[17],
M Goffe[7], J Goldstein[17], A Golubev[8], A Gorišek[9], E Grigoriev[8],
J Grosse-Knetter[23], A Grummer[21], B Gui[13], M Guthoff[3], B Hiti[9], D Hits[24],
M Hoeferkamp[21], T Hofmann[3], J Hosselet[7], J-Y Hostachy[27], F Hügging[1],
C Hutton[17], J Janssen[1], H Kagan[13], K Kanxheri[28], G Kasieczka[24],
R Kass[13], M Kis[5], G Kramberger[9], S Kuleshov[8], A Lacoste[27],
S Lagomarsino[4], A Lo Giudice[15], I Lopez Paz[22], E Lukosi[25], C Maazouzi[7],
I Mandic[9], C Mathieu[7], M Menichelli[28], M Mikuž[9], A Morozzi[28], J Moss[29],
R Mountain[20], A Oh[22], P Olivero[15], D Passeri[28], H Pernegger[3],
R Perrino[26], M Piccini[28], F Picollo[15], M Pomorski[11], R Potenza[2],
A Quadt[23], F Rarbi[27], A Re[15], M Reichmann[24], S Roe[3], D A Sanz Becerra[24],
M Scaringella[4], D Schaffner[24], C J Schmidt[5], S Schnetzer[14], E Schioppa[3],
S Sciortino[4], A Scorzoni[28], S Seidel[21], L Servoli[28], D S Smith[13], B Sopko[18],
V Sopko[18], S Spagnolo[26], S Spanier[25], K Stenson[19], R Stone[14], C Sutera[2],
M Traeger[5], W Trischuk[16], M Truccato[15], C Tuve[2], J Velthuis[17], N Venturi[3],
S Wagner[19], R Wallny[24], J C Wang[20], J Weingarten[23], C Weiss[3],
T Wengler[3], N Wermes[1], M Yamouni[27] and M Zavrtanik[9] (The RD42
Collaboration)[3]

1 Universität Bonn, Bonn, Germany
2 INFN/University of Catania, Catania, Italy
3 CERN, Geneva, Switzerland
4 INFN/University of Florence, Florence, Italy
5 GSI, Darmstadt, Germany
6 Ioffe Institute, St. Petersburg, Russia
7 IPHC, Strasbourg, France
8 ITEP, Moscow, Russia
9 Jožef Stefan Institute, Ljubljana, Slovenia
10 Universität Karlsruhe, Karlsruhe, Germany
11 CEA-LIST Technologies Avancées, Saclay, France
12 MEPHI Institute, Moscow, Russia
13 The Ohio State University, Columbus, OH, United States of America

30 Author to whom any correspondence should be addressed.

[14] Rutgers University, Piscataway, NJ, United States of America
[15] University of Torino, Torino, Italy
[16] University of Toronto, Toronto, ON, Canada
[17] University of Bristol, Bristol, United Kingdom
[18] Czech Technical University, Prague, Czech Republic
[19] University of Colorado, Boulder, CO, United States of America
[20] Syracuse University, Syracuse, NY, United States of America
[21] University of New Mexico, Albuquerque, NM, United States of America
[22] University of Manchester, Manchester, United Kingdom
[23] Universität Göttingen, Göttingen, Germany
[24] ETH Zürich, Zürich, Switzerland
[25] University of Tennessee, Knoxville, TN, United States of America
[26] INFN-Lecce, Lecce, Italy
[27] LPSC-Grenoble, Grenoble, France
[28] INFN-Perugia, Perugia, Italy
[29] California State University, Sacramento, CA, United States of America

E-mail: lukas.baeni@cern.ch

CrossMark

Abstract

We have measured the radiation tolerance of poly-crystalline and single-crystalline diamonds grown by the chemical vapor deposition (CVD) process by measuring the charge collected before and after irradiation in a 50 μm pitch strip detector fabricated on each diamond sample. We irradiated one group of sensors with 800 MeV protons, and a second group of sensors with 24 GeV protons, in steps, to $(1.34 \pm 0.08 \times 10^{16})$ protons cm^{-2} and $(1.80 \pm 0.18 \times 10^{16})$ protons cm^{-2} respectively. We observe the sum of mean drift paths for electrons and holes for both poly-crystalline CVD diamond and single-crystalline CVD diamond decreases with irradiation fluence from its initial value according to a simple damage curve characterized by a damage constant for each irradiation energy and the irradiation fluence. We find for each irradiation energy the damage constant, for poly-crystalline CVD diamond to be the same within statistical errors as the damage constant for single-crystalline CVD diamond. We find the damage constant for diamond irradiated with 24 GeV protons to be $0.62 \, ^{+0.01}_{-0.01}$ (stat) $^{+0.06}_{-0.06}$ (syst) $\times 10^{-18}$ cm^2 ($p \, \mu$m)$^{-1}$ and the damage constant for diamond irradiated with 800 MeV protons to be $1.04 \, ^{+0.02}_{-0.02}$ (stat) $^{+0.04}_{-0.05}$ (syst) $\times 10^{-18}$ cm^2 ($p \, \mu$m)$^{-1}$. Moreover, we observe the FWHM/MP pulse height decreases with fluence for poly-crystalline CVD material and within statistical errors does not change with fluence for single-crystalline CVD material for both 24 GeV proton irradiation and 800 MeV proton irradiation. Finally, we have measured the uniformity of each sample as a function of fluence and observed that for poly-crystalline CVD diamond the samples become more uniform with fluence while for single-crystalline CVD diamond the uniformity does not change with fluence.

Keywords: chemical vapor deposition, single crystal diamond, polycrystalline diamond, charge collection distance, mean drift path, radiation tolerance, radiation damage constant

(Some figures may appear in colour only in the online journal)

1. Introduction

Radiation tolerance, to varying degrees, is required for most modern experiments in accelerator physics, high energy physics, nuclear physics, synchrotron x-ray physics and space physics. In most of these areas of physics, the detectors closest to the source or interaction point usually receive the largest radiation dose. For example, devices at the present Large Hadron Collider (LHC) at CERN [1] must remain operational after a fluence of roughly 10^{15} particles cm^{-2} in order for the experiments (e.g. ATLAS and CMS) to perform satisfactorily [2]. For future experiments at CERN, it is expected that the innermost detectors will accumulate an order of magnitude larger fluence [3, 4]. This trend of increasing required radiation tolerance is now common in areas where sources and beams are developed with higher energy or higher intensity to

J. Phys. D: Appl. Phys. **52** (2019) 465103

L Bäni *et al*

Table 1. Properties of diamonds irradiated with 800 MeV protons and the fluence they received. The initial *ccd* values are given separately for positive and negative bias polarity.

Diamond	Type	Thickness (μm)	Area (mm^2)	*ccd* (μm)	Fluence (10^{15} p cm^{-2})
Sample 1	pCVD	516	10×10	230/227	0
					12.6 ± 1.3
Sample 2	pCVD	510	10×10	218/228	0
					3.5 ± 0.4
Sample 3	pCVD	511	10×10	227/241	0
					5.5 ± 0.6
					10.3 ± 0.7
Sample 4	scCVD	466	5×5	466/466	0
					0.78 ± 0.07
					2.38 ± 0.18
					3.05 ± 0.19
					7.8 ± 0.5
					13.4 ± 0.8

Table 2. Properties of diamonds irradiated with 24 GeV protons and the fluence they received. The initial *ccd* values are given separately for positive and negative bias polarity.

Diamond	Type	Thickness (μm)	Area (mm^2)	*ccd* (μm)	Fluence (10^{15} p cm^{-2})
Sample 5	pCVD	490	10×10	239/239	0
					5.9 ± 0.6
					18.0 ± 1.8
Sample 6	scCVD	465	5×5	465/465	0
					1.38 ± 0.08
					2.83 ± 0.13
Sample 7	scCVD	395	5×5	395/395	0
					1.47 ± 0.07

reach new regimes of physics. As a result, an enormous effort is ongoing to find detector materials that operate after fluences of $>10^{16}$ particles cm^{-2}.

The large displacement energy of diamond [5, 6], which enhances its inherent radiation tolerance, allows diamond to be a candidate for such a material. During the past few years, the RD42 Collaboration [7] at CERN has developed chemical vapor deposition (CVD) diamond for detector use in very high radiation environments. Based in part on the RD42 results [8, 9] as well as the results of other groups [10–12], CVD diamond detectors have been proposed and used in radiation areas where silicon use is marginal. For example, in beam monitoring systems, where cooling is difficult and radiation levels are high, diamond use has already superseded silicon use. In this area CVD diamond based beam condition monitors are now (or were) in use in BaBar [13–15], CDF [16, 17], ATLAS [18, 19], CMS [20, 21] and LHCb [22].

The RD42 collaboration has spent the last several years investigating the radiation tolerance of CVD diamond. This article describes the 800 MeV proton irradiations performed at the Los Alamos LANSCE facility[31] and the 24 GeV proton

irradiations performed at the CERN IRRAD facility[32] used to measure the radiation tolerance of poly-crystalline CVD (pCVD) diamond and single-crystalline CVD (scCVD) diamond, the beam tests of non-irradiated and irradiated detectors and the analysis of test beam data used to quantify the radiation tolerance. There are five new results presented in this work. First, we observe the sum of mean drift paths for electrons and holes for both pCVD and scCVD diamond decreases with irradiation fluence from its initial value (λ_0) according to the damage curve $1/\lambda = 1/\lambda_0 + k_i \times \phi$, where k_i is the damage constant for irradiation beam energy i and ϕ is the irradiation fluence. Second, we find the damage constant, k_i, for pCVD diamond to be the same within statistical errors as that for scCVD diamond. Third, the new measurement of the damage constant we have performed for diamond irradiated with 24 GeV protons and 800 MeV protons is the most precise to date by the RD42 collaboration. We find the damage constant for diamond irradiated with 24 GeV protons to be $0.62 ^{+0.01}_{-0.01}$ (stat) $^{+0.06}_{-0.06}$ (syst) $\times 10^{-18}$ cm^2 $(p$ μm$)^{-1}$ and the damage constant for diamond irradiated with 800 MeV protons to be $1.04 ^{+0.02}_{-0.02}$ (stat) $^{+0.04}_{-0.05}$ (syst) $\times 10^{-18}$ cm^2 $(p$ μm$)^{-1}$. Fourth, from the evolution of the pulse height distributions of each sample as a function of fluence, we observe the full width at half maximum divided by the most probable pulse

---

[31] For information about the Los Alamos National Laboratory LANSCE Blue Room irradiation facility see http://wnr.lanl.gov/. Additional information is available at: http://panda.unm.edu/NUPAC_NMCPP/atlas_pixel/research/pages/documents/Beam_Profile_UNM.pdf.

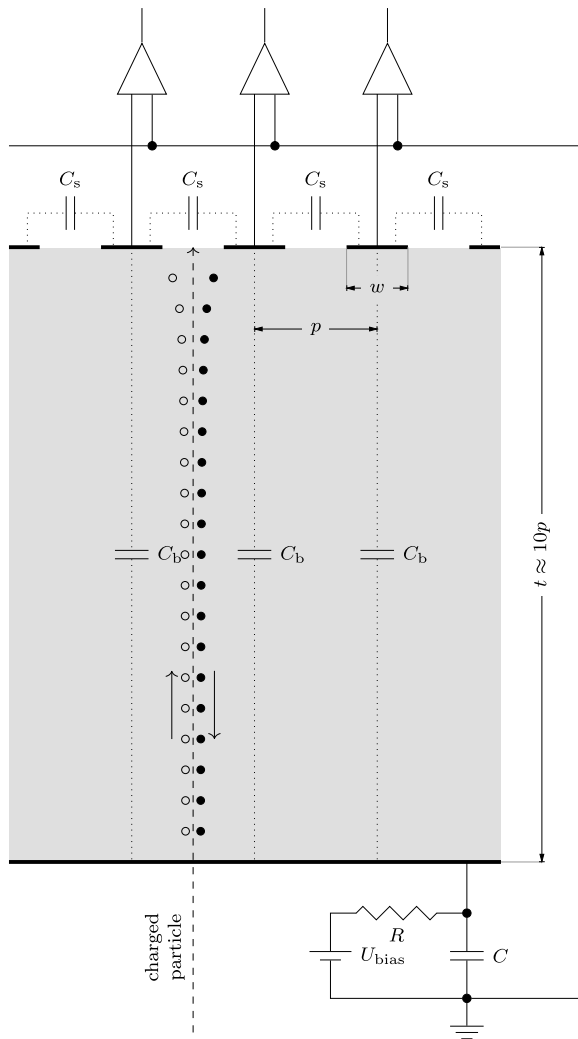[32] For information about the CERN IRRAD irradiation facility: https://ps-irrad.web.cern.ch/description.php.

J. Phys. D: Appl. Phys. **52** (2019) 465103

L Bäni *et al*

Figure 1. A schematic view of a diamond strip detector. The capacitances between strips and from the strips to the backplane electrode, C_s and C_b, are shown. The strip width, w, is 25 μm. Each strip is connected to an individual amplifier channel. The strip pitch, p, is 50 μm. The thickness of the detector material, t, is roughly 500 μm or $\sim 10 \times p$. The external high voltage, U_{bias}, is applied to the backplane electrode through an RC filter circuit.

height decreases with fluence for pCVD material and is within statistical errors flat with fluence for scCVD material for both 24 GeV proton irradiations and 800 MeV proton irradiations. Fifth, we have measured the uniformity of each sample as a function of fluence and observe that for pCVD diamond the samples become more uniform with fluence while for scCVD diamond the uniformity does not change with fluence.

2. Sample description and device preparation

There are two types of CVD diamond used in this investigation. The first is single-crystalline which, as the name implies, is ideally one single diamond crystal devoid of grains and grain boundaries. High purity single-crystalline material has the ability to collect the full charge deposited in the material but the material area is currently limited to $\sim 7 \times 7$ mm. The second is poly-crystalline which is made up of a collection of randomly oriented crystals implying the material has

individual grains and grain boundaries. In poly-crystalline material, the collected charge is less than the deposited charge due to grain boundaries, dislocations and traps in the material. A high quality, 500 μm thick, pCVD diamond collects approximately half of the deposited charge but can be grown in very large areas up to 15 cm diameter wafers. In order to quantify the radiation tolerance of pCVD diamond and scCVD diamond, we irradiated a series of poly-crystalline and single-crystalline samples with various properties (type, thickness, area, non-irradiated charge collection) with 800 MeV protons and 24 GeV protons. Table 1 shows the properties of the diamonds irradiated with 800 MeV protons and the fluence they received. Table 2 shows the properties of the diamonds irradiated with 24 GeV protons and the fluence they received.

To test each diamond after irradiation, a 50 μm pitch strip detector, typically with 32- or 64-strips, was fabricated on each sample. In figure 1, we show the basic principle of using diamond as a strip detector. A voltage is applied across a layer of diamond a few hundred microns thick. When a charged particle traverses the diamond, atoms in crystal lattice sites are ionized, promoting electrons into the conduction band and leaving holes in the valence band. On average, 3600 electron–hole pairs are created per 100 μm of diamond traversed by a minimum ionizing particle [23], independent of the type of diamond material (pCVD or scCVD). These charges drift across the diamond in response to the applied external electric field inducing a signal on a number of strips which can be measured. For detectors of the thickness used in this experiment, fluctuations in the energy loss of traversing particles occur. The energy loss probability distribution can be expressed by the Landau–Vavilov distribution [24, 25] with the density correction by Bichsel [26]. Due to the fact that the energy deposition depends on the characteristics of the incident particle and the intrinsic material [27], one expects that, on average, the same charge is generated in scCVD and pCVD diamond. Since there may be traps in the material, we use the term 'charge collection distance' (*ccd*) to denote the average distance the electron–hole pairs drift apart under the influence of the applied external electric field. The grain boundaries of a pCVD diamond may act like charge traps in the material. Therefore, the measured signal in pCVD diamond is expected to be smaller than that in an scCVD diamond.

In preparing the diamond devices for testing, the same strip width and strip detector pitch was used for both pCVD and scCVD diamond. The bias side was fabricated using photolithographic techniques with a single pad. The readout side was fabricated with photolithographic techniques with 25 μm wide strips with a 25 μm gap between strips producing a device with 50 μm pitch. The strip pattern was enclosed with a guard ring at the same potential as the strips to minimize any edge or surface currents from being picked up by the individual electronic channels. After metalization of both sides with 500 Å Cr and 2000 Å Au, each device was annealed at 400 °C for 4 min in an N_2 atmosphere. The bias electrode side of the device was attached with silver paint [28] to a ceramic hybrid containing a bias pad and RC bias filter circuit to power the device. The ceramic hybrid was mounted adjacent to a G-10 printed circuit board which housed the IDE AS VA2.2

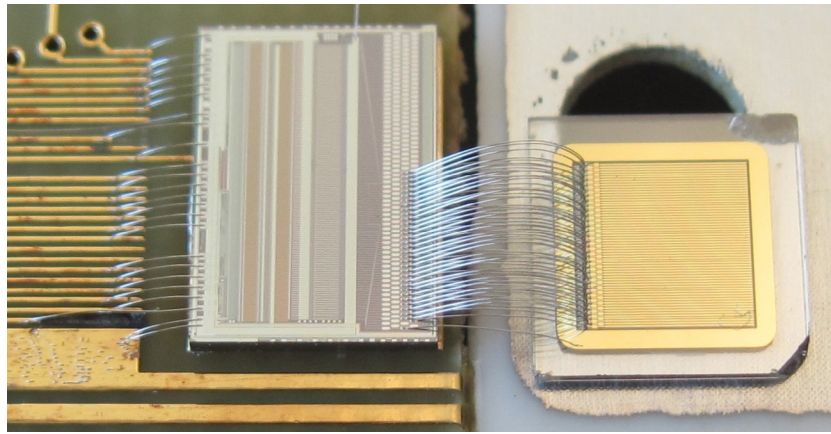J. Phys. D: Appl. Phys. **52** (2019) 465103

L Bäni *et al*

Figure 2. Photograph of the sample 4 diamond strip detector mounted on a ceramic hybrid (right portion of the figure) and wirebonded to VA2.2 readout electronics (left portion of the figure).
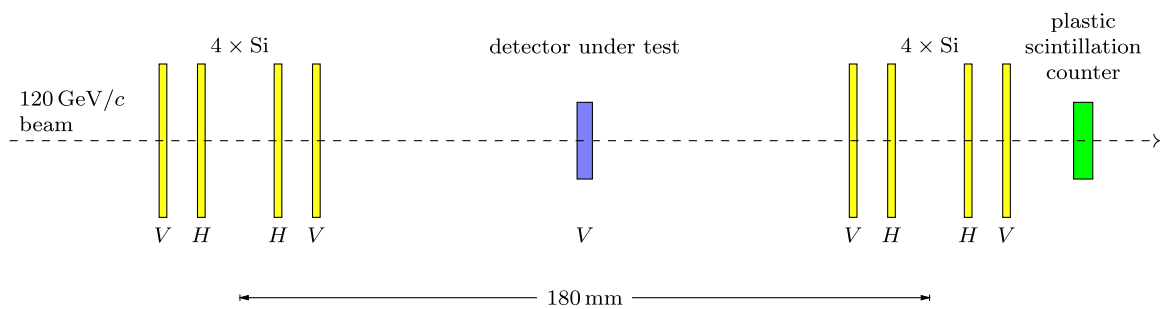

Figure 3. Schematic view of the eight plane 'Strasbourg' telescope used to identify candidate tracks which pass through the detector under test. The planes are identified as *V* for vertical strips (providing a measurement of the *x* coordinate) and *H* for horizontal strips (providing a measurement of the *y* coordinate). The telescope was triggered by a signal in a 7×7 mm plastic scintillation counter.

readout chip [29] so each readout strip could be directly wire bonded from the diamond strip detector to a VA2.2 readout channel. Figure 2 shows a picture of the sample 4 diamond sensor mounted on a ceramic printed circuit board and wire bonded to the VA2.2 readout electronics.

3. Device setup and readout

The diamond devices, both non-irradiated and irradiated, were read out using the VA2.2 readout chip with a 1.8 μs peaking time and characterized using a high precision tracking telescope [30] in a 120 GeV hadron beam at CERN. This method allowed the matching of charge deposition in the diamond with beam particle trajectories. Since the VA2.2 readout chip is not radiation hard the diamonds were removed from the ceramic hybrid and the metal was stripped in order to perform each irradiation step. As a result, each beam test was performed using unused VA2.2 readout channels. This method required lab and test beam calibration in order to be able to compare the results at various fluences. The lab calibration was performed by first 'pumping' the diamond with a 37 MBq ^{90}Sr β-source 1 cm from the sample for 15 h to put the diamond in a stable state by filling unfilled traps. The pulse height from a given sample was determined using a setup with a ^{90}Sr β-source providing particles which pass through the

sample and are triggered with an external scintillator placed behind diamond. The pulse height was measured for every external trigger using the same VA readout electronics that was used in the test beam. The gain and noise of every channel were measured. In addition, each device was verified to hold high voltage of at least ± 1000 V before the test beam began to avoid any data taking problems during the test beam, such as large leakage currents that could saturate the VA2 single channel amplifiers.

4. Sample irradiations

Samples 1–4 were irradiated in the blue room of the Los Alamos LANSCE irradiation facility in multiple steps in order to measure the radiation tolerance of CVD diamond material to 800 MeV protons as a function of fluence. The fluence was quantified by measuring the activity of ^{22}Na isotope in an aluminum foil placed either directly in front or directly behind each sample. The details of the full procedure may be found in [31]. The results of this procedure for the 800 MeV irradiations are listed in table 1.

Samples 5–7 were irradiated in the IRRAD proton facility located on the T8 beam-line at the CERN Proton Synchrotron (PS) East Hall at CERN in Switzerland. At this facility, the primary proton beam with a momentum of 24 GeV c^{-1} is extracted from the PS ring. Samples were mounted in slide
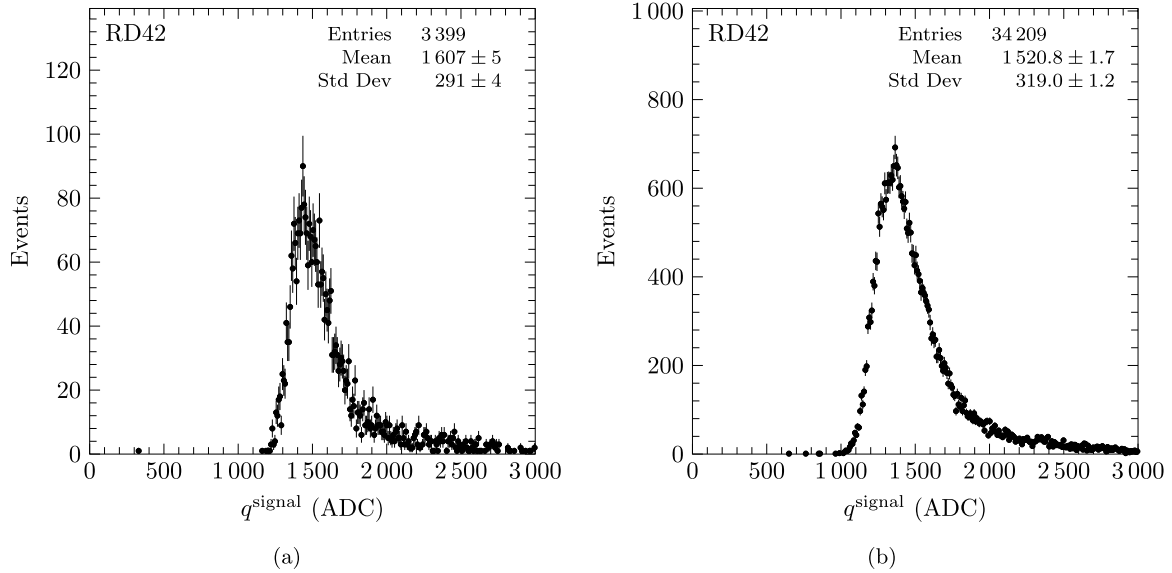
Figure 4. The single-crystal calibration. (a) The thickness of the scCVD diamond is 565 μm and the mean ADC count is 1607 yielding a calibration of $ADC_{cal} = 7.90$ ADC/100e. This value of ADC_{cal} is near in the middle of the distribution of calibration constants. (b) The thickness of the scCVD diamond is 466 μm and the mean ADC count is 1521 yielding a calibration of $ADC_{cal} = 9.07$ ADC/100e. This value of ADC_{cal} is the high extreme of the distribution of calibration constants.

holders along the beamline. The flux was measured by secondary emission chambers (SECs) and recorded. The beam position was monitored using a luminescence screen and a camera. The absolute proton fluence was measured by the radiation group at CERN using the aluminum foil activation method similar to that described above. The results of this procedure for the 24 GeV irradiation are listed in table 2.

5. Data taking procedure of diamond signal response

Each diamond sample was characterized by measuring the charge created by 120 GeV hadrons in a test beam at CERN before and after irradiation. The 'Strasbourg' telescope was used to provide tracking information of the incident hadron beam. This telescope [30] consists of four pairs of x and y planes of silicon detectors each 12.8 mm $\times$ 12.8 mm $\times$ 300 μm thick. The eight silicon planes each have 50 μm pitch with floating intermediate strips. Each plane has 256 strips and is read out with two VA2 ASICs with a 1.2 μs shaping time. The telescope was read out when the signals from two photomultipliers viewing a 7 $\times$ 7 mm scintillation counter coincided. An overall view of the 'Strasbourg' telescope is shown in figure 3.

Before each diamond was mounted in the 'Strasbourg' telescope for testing the diamond was put into the stable state it would be in during data taking at any high luminosity collider by 'pumping' it with a 54 MBq ^{90}Sr β-source to fill unfilled traps. The data taking protocol consisted of

- 4 h pumping with a 54 MBq ^{90}Sr β-source 1 cm from the sample,
- collecting data (typically 400 000 events) at low positive voltage (typically +400 V to +500 V corresponding to $E = 1$ V μm^{-1}),

- collecting data (typically 1 000 000 events) at high positive voltage (typically +800 V to +1100 V corresponding to $E = 2$ V μm^{-1}),
- 4 h pumping with a 54 MBq ^{90}Sr β-source 1 cm from the sample,
- collecting data (typically 400 000 events) at low negative voltage (typically −400 V to −500 V corresponding to $E = -1$ V μm^{-1}),
- collecting data (typically 1 000 000 events) at high negative voltage (typically −800 V to −1100 V corresponding to $E = -2$ V μm^{-1}).

6. Test beam analysis

The raw recorded signal in channel i, q_i^{raw}, consists of multiple components:

$$q_i^{raw} = q_i^{hit} + q_i^{noise} + q_i^{ped} + q^{CMN} \quad (1)$$

where q_i^{hit} is the physical signal caused by a hit in the detector, q_i^{noise} is the random noise on channel i, q_i^{ped} is the pedestal of channel i and q^{CMN} is the common mode shift of the pedestal value. Since the random noise cannot be subtracted, $q_i^{signal} = q_i^{hit} + q_i^{noise}$ denotes the reconstructed signal of channel i. The first step in the analysis is the estimation of the pedestals followed by the creation of clusters. After a rough alignment, in which the first x and y planes were fixed and perpendicular straight tracks were assumed, events were chosen that had a single cluster in each of the eight silicon planes forming a straight track with a χ^2 less than four. After event selection the alignment was performed for each silicon plane and the diamond detector under test separately using the first 100 000 events of each run. The final step of the analysis
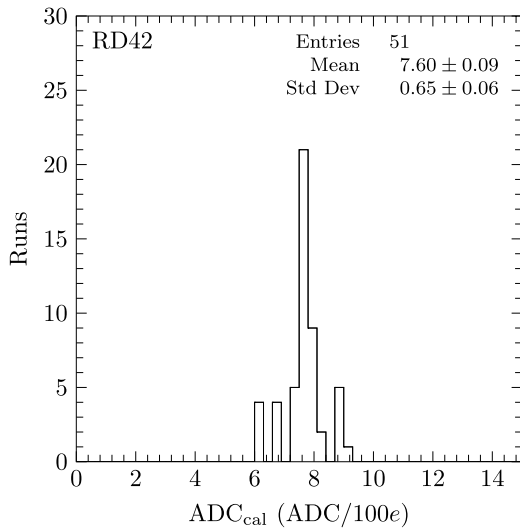
J. Phys. D: Appl. Phys. **52** (2019) 465103

L Bäni *et al*

Figure 5. The ADC$_{cal}$ constants used in the 51 data sets. The ADC$_{cal}$ calibration constant distribution has a standard deviation of 8.6% of the mean value indicating the stability of the data taking procedure and method used which spanned many years.

consisted of forming the pulse height from the detector under test for both a transparent analysis and a clustered analysis. In the transparent analysis, the five closest strips to the projected track were used in the pulse height determination while in the clustered analysis, clusters were formed from the hits in the detector under test, independent of the telescope tracks, and used in the analysis. The original 24 GeV proton irradiation data were previously analyzed using a different algorithm. The results of that analysis may be found in [32, 33]. The original data was reanalyzed in this work if that data were taken at high electric fields as described above. In this work we have expanded the original 24 GeV irradiation data set by taking additional data from the original samples to ensure all data analyzed had the same electric field values, has both positive and negative electric fields and used the updated analysis. The data sets which had original and new data were only combined after verifying the reproducibility of the original data. The features different in the updated analysis are the use of common-mode correction to reduce the noise, accounting for electronic cross-talk, and using the charge from five strips (instead of two strips) to ensure that >90% of the deposited charge was analyzed for each fluence. The full details of the updated analysis may be found in [34, 35].

6.1. Pulse height calibration

For each run the calibration of ADC channels to electrons (ADC$_{cal}$) was accomplished in one of three ways. The first method involved using a non-irradiated single-crystal diamond connected to the same VA2.2 ASIC as the detector under test. In this method, the ADC$_{cal}$ simply involved associating the ADC count from the non-irradiated single-crystal calibration detector with the thickness of the material, t:

$$\mathrm{ADC_{cal}}(\mathrm{ADC}/100e) = \mathrm{ADC} \times \frac{1}{t(\mu m)} \times \frac{1\,\mu m}{36e} \times 100.$$

Figure 4 shows the pulse height distribution of two scCVD calibration diamonds. The gain variation of different channels in the VA2.2 ASIC was less than 1% and in figure 4 the data from all channels, after pedestal alignment, have been added together. Three different scCVD diamonds were used with this method to calibrate 14 of the 51 datasets.

The second method consisted of putting a voltage step (V) on a precision capacitor (C) connected to one channel of the VA2.2 circuit. The precision capacitor was a 1% 1.8 pF capacitor. The input charge was calculated using:

$$V = \frac{Q}{C}$$

and correlated with the resultant ADC value. Using this method, 32 of the 51 datasets were calibrated.

The third method involved measuring the noise in the lab before the beam test and obtaining the ratio of the noise in the detector under question to that of a detector previously measured in a beam test. The ADC to electron calibration was then determined by:

$$\mathrm{ADC_{cal}}(\mathrm{ADC}/100e) = \mathrm{ADC_{cal}^{ref}} \times \frac{\mathrm{Noise_{test}}}{\mathrm{Noise_{ref}}}.$$

The remaining five data sets used this method.

The calibration constant, ADC$_{cal}$, for all 51 data sets is shown in figure 5. The ADC$_{cal}$ calibration constants were taken over a period of years and have a standard deviation of 8.6% of the mean value which demonstrates the stability of the procedures used.

6.2. Pedestal and noise calculation

A typical low voltage run consisted of 400k triggers and took about 1.5 h while a typical high voltage run had 1M triggers and took about 4 h. The events recorded were processed to reconstruct single particle tracks in the silicon telescope. Since there is no zero signal suppression (all channels are read out for each trigger) in the VA2 ASIC it is important to find a good estimate of the pedestal for each channel. The first 500 events were used to calculate an initial pedestal and width (σ_i) for each channel. Once the initial pedestals were determined, the pedestals for each channel were updated throughout the run using a 500 event sliding window algorithm. For each event only channels with pulse height less than $5\sigma_i$ from the pedestal were included in the sliding window pedestal algorithm (i.e. signals from charged particles were excluded). Pedestals for each channel were then available for each event throughout the run. Using the sliding window pedestals, the raw recorded signals were pedestal subtracted and corrected for common mode noise. The total noise of each individual channel was the sum of random electronic noise plus common mode noise on that channel. The total noise was determined after pedestal subtraction from the width of the pedestal distribution. The average total noise for all channels was observed to be between 92.2e and 138.6e for the 51 data sets taken. The total noise distribution for the 51 runs used is shown in figure 6(a).
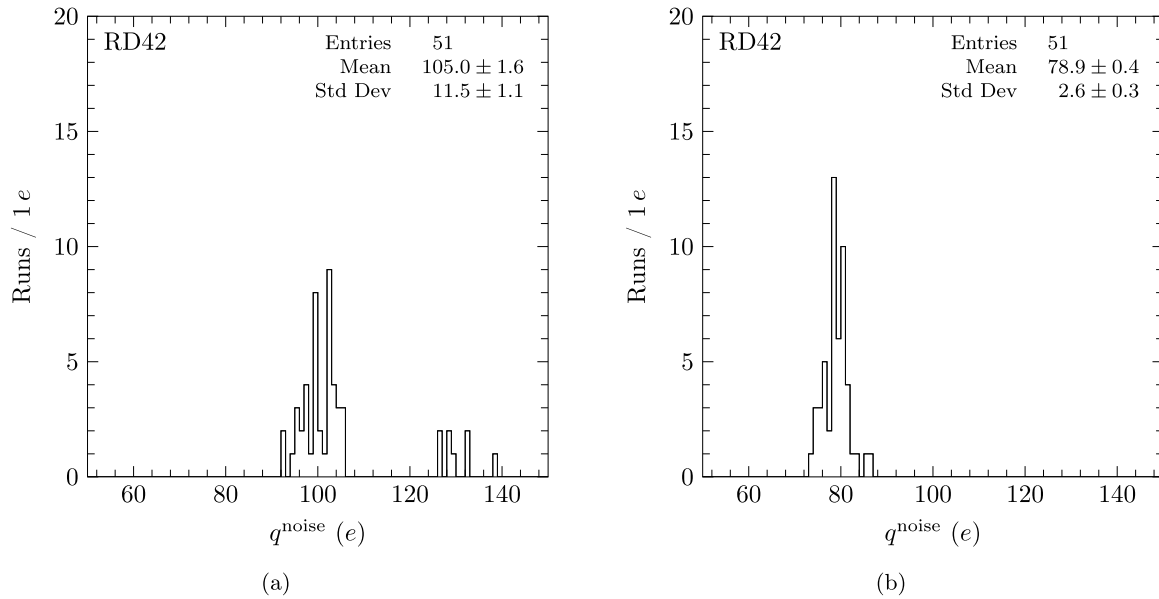
Figure 6. (a) The total noise observed in the 51 data sets and (b) the random noise (common mode corrected (CMC) total noise) observed in the 51 data sets.

For some of the data runs, the total noise was observed to exhibit a large common mode component. In order to include that data, a common mode correction (CMC) algorithm was implemented for all runs. In this algorithm, for each event, the mean ADC channel and standard deviation for all strips in the detector was calculated and compared against the historical mean and standard deviation of the last 256 events. The difference of the event mean and the historical mean was subtracted from all channels. This algorithm yielded, for the same runs shown in figure 6(a), the CMC noise distribution shown in figure 6(b). The CMC noise distribution is a good representation of the random noise distribution where the CMC noise distribution ranges from $73.2e$ to $86.6e$. The standard deviation of the noise distributions was reduced from $11.5e$ for the total noise distribution to $2.6e$ for the CMC noise distribution (random noise distribution). The random noise obtained after CMC was checked for consistency with that expected from the VA2.2 circuit[33] with a 1.8 μs peaking time, i.e. the CMC noise is expected to be between $70e$ and $90e$ for a 50 μm pitch strip detector in diamond. This condition was met for all 51 data sets as shown in figure 6(b).

6.3. Track selection

Once the CMC noise was determined the functionality of all diamond channels was verified by looking for hits with signals larger than 5σ CMC noise. Non-working, non-functional channels were excluded from the remaining analysis. The average number of excluded channels per run in the 51 data sets was 16% due to all issues including high noise, noise lower than the VA specifications indicating a non-properly functioning channel and broken wire bonds.

After aligning the telescope, tracks to study the detector under test were reconstructed. To simplify the combinatorics

in the reconstruction, only events with a single cluster with signal seed greater than $5\sigma_i$ above the noise in each silicon plane were used. A track was fit as a straight line through the hit positions in the silicon planes, separately for x and y directions. The fitted tracks were used to determine the average intrinsic resolution of each telescope plane by removing that telescope plane from the track reconstruction. The average intrinsic resolution of the telescope planes was determined in this way to be 1.8 μm. Since a beam of high energy particles (120 GeV) was used, only a minor contribution due to multiple scattering was expected. To eliminate any mistracking, delta rays or small angle multiple scattering events, tracks were required to have a goodness of fit of $\chi^2/N_{\text{dof}} < 4/2$ in both x and y. On average, 46% of the tracks were rejected by this χ^2/N_{dof} requirement. After the χ^2/N_{dof} requirement in both x and y, the uncertainty on the predicted hit position in the detector under test was roughly 1.3 μm in both x and y.

6.4. Transparent and cluster analysis

Once a track from the telescope was reconstructed, the intercept of that track with the detector under test was identified as the *predicted* hit position. In the transparent analysis, N strips around the predicted hit position were considered (N was taken to be 10 in this work to account for the charge spreading in heavily irradiated detectors). M contiguous strips of the N strips considered were chosen around the strip with the largest pulse height to form an *M/N transparent cluster*. All N strips were required to lie within a predetermined fiducial region. For the transparent charge in this analysis M was 5 and N was 10. For the *cluster analysis*, a seed strip was determined as $>5\sigma$ above the CMC noise for that strip. The seed strip was determined independent of the predicted hit position. Additional hit strips were added to the cluster as long as the additional strips were adjacent to the seed strip and had a charge $>3\sigma$ above the CMC noise. On average, 34% of the events in diamond

---

[33] The VA2.2 specs are $80e + 15e$/pF rms for 1 μs peaking time and $60e + 11e$/pF rms for 2 μs peaking time. The full VA2.2 specs are given in [36].
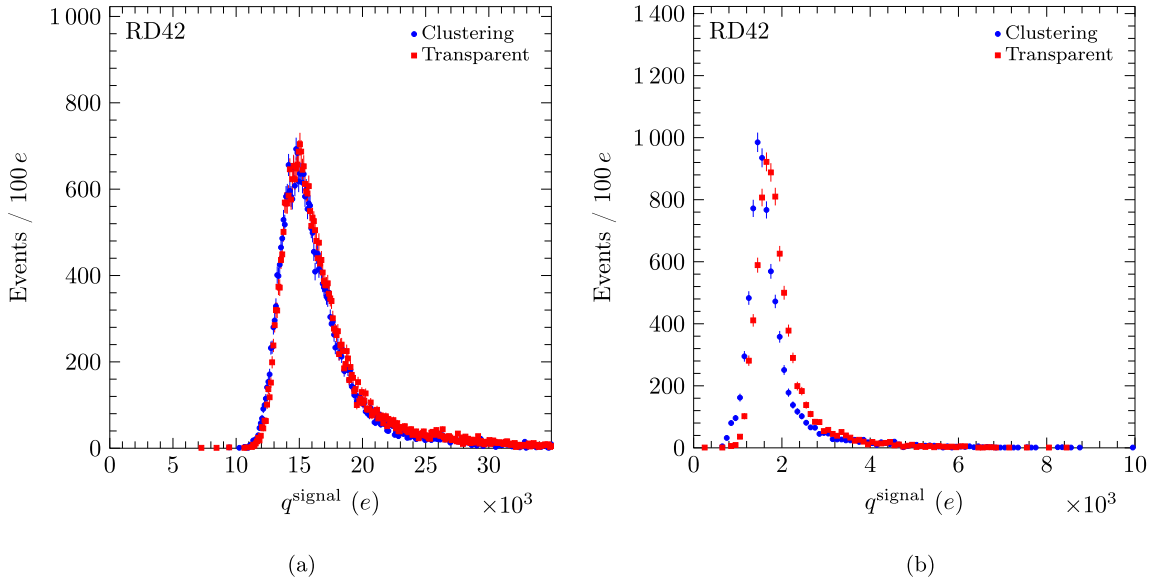
(a)

(b)

Figure 7. The signal charge distributions reconstructed with transparent and clustered algorithms (a) non-irradiated and (b) after an 800 MeV proton fluence of 13.4×10^{15} p cm^{-2} for sample 4.

Table 3. Systematic uncertainties of the signal charge.

Source of uncertainty	Uncertainty (%)		
	Transparent	Clustered	Source
Calibration	4.0	4.0	5–10
Signal stability (time)	0.1–8.5	1–6	—
Signal stability (position)	1–10	—	—
Signal reproducibility	0.5–0.6	0.5–0.6	—
Charge offset	—	—	4.0

were 1-strip events, 35% of the events in diamond were 2-strip events, 14% of the events in diamond were 3-strip events, 9% of the events in diamond were 4-strip events and 7.1% of the events in diamond had greater than 4-strips. These numbers depend on the choice of seed and hit definitions and the fluence the device has received.

The q^{signal} was calculated in ADC units by summing the largest signals in the detector under test around the projected track from the tracking telescope:

$$q^{\text{signal}} = \sum_{i \in C} q_i^{\text{signal}} \qquad (2)$$

where C is the set of selected five strips in ten for the transparent analysis and $C = \{1, 2, 3, 4, \ldots\}$ for the different cluster analyses possible. Figure 7 shows the signal charge distributions for the same events with the 5/10 transparent and 1–5-strip cluster algorithms before and after an 800 MeV proton fluence of 13.4×10^{15} p cm^{-2}. In all cases the transparent algorithm gives a larger mean charge than the cluster algorithm.

The ccd was calculated from the signal charge (in ADC units) by:

$$ccd = q^{\text{signal}} \times \frac{100}{\text{ADC}_{\text{cal}}} \times \frac{1 \, \mu\text{m}}{36e}. \qquad (3)$$
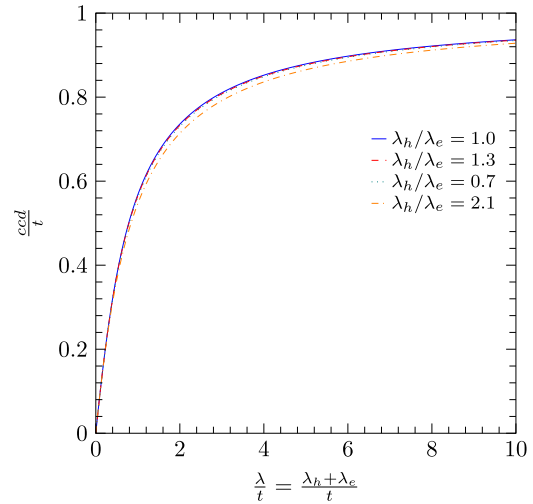

Figure 8. The relation between ccd/t and λ/t for the ratios $\lambda_h/\lambda_e = 1.0, 1.3, 0.7$ and 2.1. This figure indicates the effect due to not knowing the λ_h/λ_e ratio is small as long as the ratio is within the range plotted.

The two main systematic uncertainties in this analysis are from the calibration constants ADC_{cal} and the pulse height dependence on time and track position. The calibration constants described in section 6.1 were determined with an uncertainty of 4% which is assigned as systematic uncertainty on the measured ccd of each run. The pulse height dependence on time and track position was determined for each run separately. In some runs, the pulse height varied systematically as a function of time due to a surface effect at the metal diamond interface [34]. The effect was reduced after properly preparing the diamond surface before metalization. For these runs, a slope was fitted to the signal as a function of time. Using the fitted slope, half of the observed difference between the beginning and end of a run was considered as a systematic uncertainty. However, for the majority of runs (45 of 51) this uncertainty is less than 3%, indicating a stable signal. To
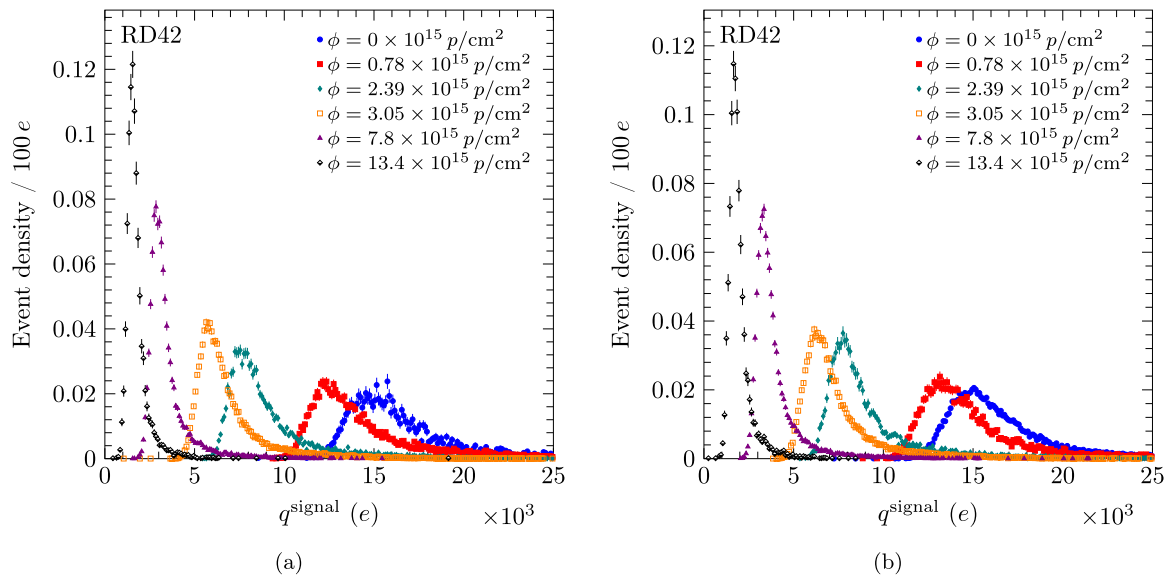
Figure 9. The pulse height evolution for (a) negative bias and (b) for positive bias for sample 4 irradiated with 800 MeV protons. The integral of each spectrum has been normalized to unity.

estimate the position dependence of the pulse height, the fiducial region was divided into subareas. On average, a variation of 3.5% was observed. The 1σ spread of the measured signal in the different subareas was assigned as systematic uncertainty on the pulse height to reflect a possible effect due to a non-uniform beam profile during the irradiation of the sample. Some of the measurements were repeated in different beam test campaigns. Based on the variation in *ccd* from these runs, a 3 μm systematic uncertainty was assigned to the *ccd* measurement of each run as a measure of the reproducibility of the conditions of a run.

The measurement procedure of the signal response to a ^{90}Sr β-source included several measurements at different bias voltages from 0 V to 1000 V, followed by a measurement cycle with negative bias polarity. Each measurement was corrected for the offset at 0 V. If the 0 V value was different for the positive and negative voltage measurements, 100% of the difference was considered as systematic uncertainty on the measured signal. Some unirradiated samples (four pCVD and one scCVD) were not characterized in a beam test. For these samples the source data was used in place of the beam test data to calculate q^{signal} and *ccd* instead.

The source of systematic uncertainties of the signal charge and their estimated values are summarized in table 3. For each run these systematic uncertainties were added in quadrature to the statistical uncertainty to obtain the total uncertainty of the measured *ccd*.

6.5. Electron and hole drift determination

To estimate the damage induced by the radiation in diamond, a simple model with a linear dependence of the radiation induced traps with fluence was used [37]. This radiation damage model can be expressed in terms of the 'schubweg', λ, the average distance a carrier traverses before being captured. The model is given by:

$$\frac{1}{\lambda} = \frac{1}{\lambda_0} + k\phi \tag{4}$$

where k is the radiation damage constant which is extracted from a fit to the data for each CVD diamond sample. The λ_0 term accounts for the inherent defects present in samples and is treated as a parameter which is also extracted from a fit to the data while λ is derived from the average measured signal charge. The average total distance the electron and hole move apart after being created, λ, which is related to the average signal charge observed by the Shockley–Ramo theorem [38, 39], is given by the sum $\lambda = \lambda_e + \lambda_h$. As the material is damaged by radiation, the number of traps increases resulting in a decrease of λ_h and/or λ_e which causes a decrease of the signal charge. The signal charge also determines the *ccd* as discussed above and so the *ccd* can be written in terms of λ_h and λ_e as [40]:

$$\frac{ccd}{t} = \sum_{i=e,h} \frac{\lambda_i}{t} \left[1 - \frac{\lambda_i}{t} \left(1 - \mathrm{e}^{-\frac{t}{\lambda_i}} \right) \right] \tag{5}$$

where t is the thickness of the material. A plot of the relation between ccd/t and λ/t is shown in figure 8 for various ratios of λ_h/λ_e. The measured mobility and lifetime values in diamond [10] indicate the schubweg ratio, λ_h/λ_e, should be $\sim$1.3. Since we do not determine the schubweg ratio λ_h/λ_e we varied the ratio, λ_h/λ_e, between 0.7 and 2.1 in order to determine the effect of this variation on the charge (*ccd*) results and the damage constant (k_i) results and included the effect as part of the systematic error on our measured values.

6.6. Damage constant fitting

The detectors under test were measured in multiple beam tests. For each device at each fluence and for each beam test individual calibration constants were determined and the observed transparent charge signal was determined using
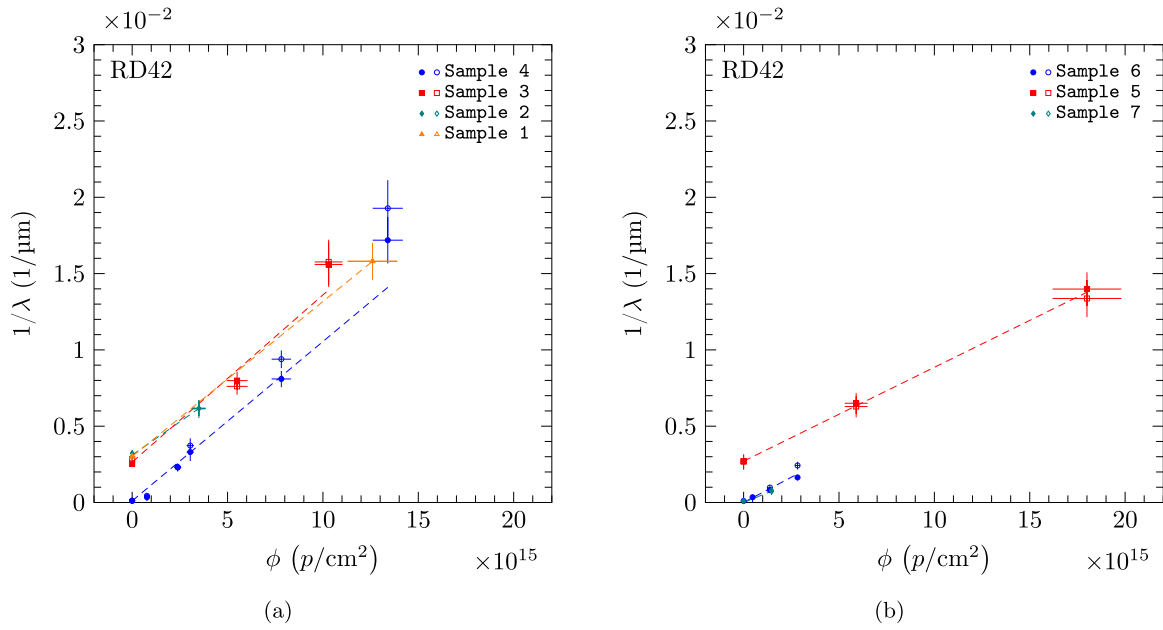
Figure 10. The $1/\lambda$ for each sample in the (a) 800 MeV irradiation and (b) 24 GeV irradiation. In this plot, the two values shown at each fluence are values for positive (solid markers) and negative (open markers) bias at $E = 2$ V μm^{-1}. Each sample was individually fit with a linear damage model.
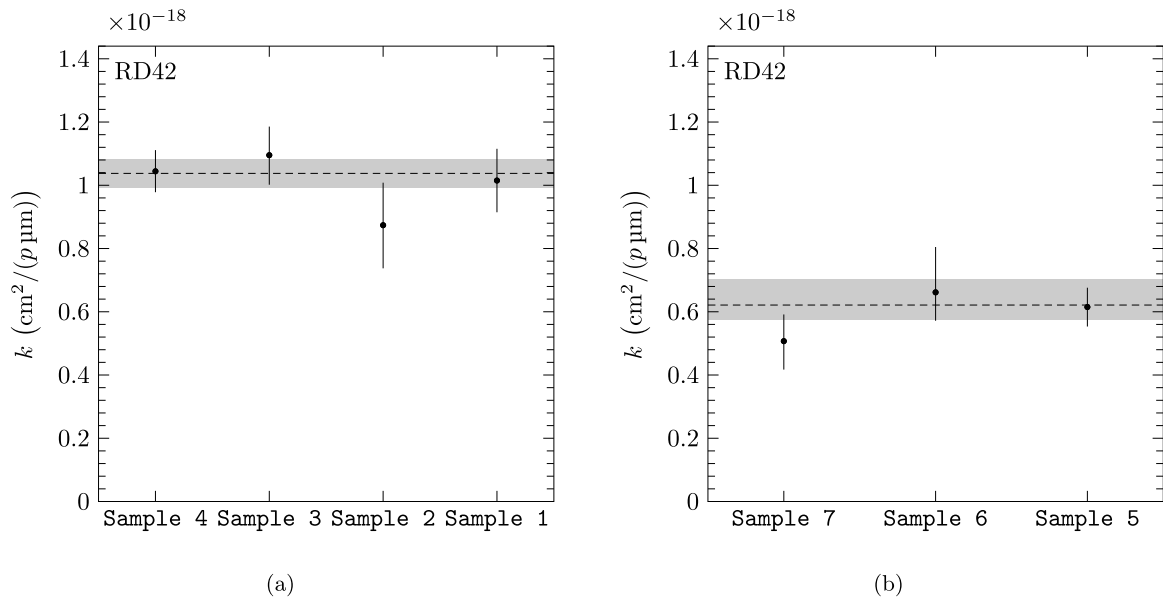

Figure 11. The damage constant results for each individual sample in the (a) 800 MeV irradiation and (b) 24 GeV irradiation. The errors are the results from the fit with only statistical errors included. The dashed lines in (a) and (b) represent a fit of a constant to the individual data points resulting in a goodness of fit χ^2/N_{dof} of (a) 2.06/3 and (b) 2.56/2. The gray band is the one standard deviation variation from each fit.

a five strips out of ten algorithm. This transparent charge signal is independent of any threshold. In figure 9(a), we show the transparent charge signal spectrum evolution for negative bias ($E = -2$ V μm^{-1}) and in figure 9(b) we show the charge signal spectrum evolution for positive bias ($E = +2$ V μm^{-1}) for all the 800 MeV proton irradiation fluences. The integral of each spectrum has been normalized to unity. At each fluence, the pulse height spectrum can be described by a Landau distribution [41] convoluted with Gaussian distributions to account for the electronic and other noise components. Figure 9 indicates two effects: (1)

for both positive and negative bias a decrease in the signal charge with increasing fluence is observed; (2) for both positive and negative bias the spectrum becomes narrower with increasing fluence.

Using the calibration constants described above the *ccd* was calculated from the signal charge and the mean drift path, λ, was determined from the *ccd*. The data from each sample was then plotted on a graph of $1/\lambda$ versus fluence and fit with a linear damage model curve of (4). In this method, the slope represents the damage constant. Figure 10(a) shows the data and the linear fits for each of the 800 MeV irradiated samples.
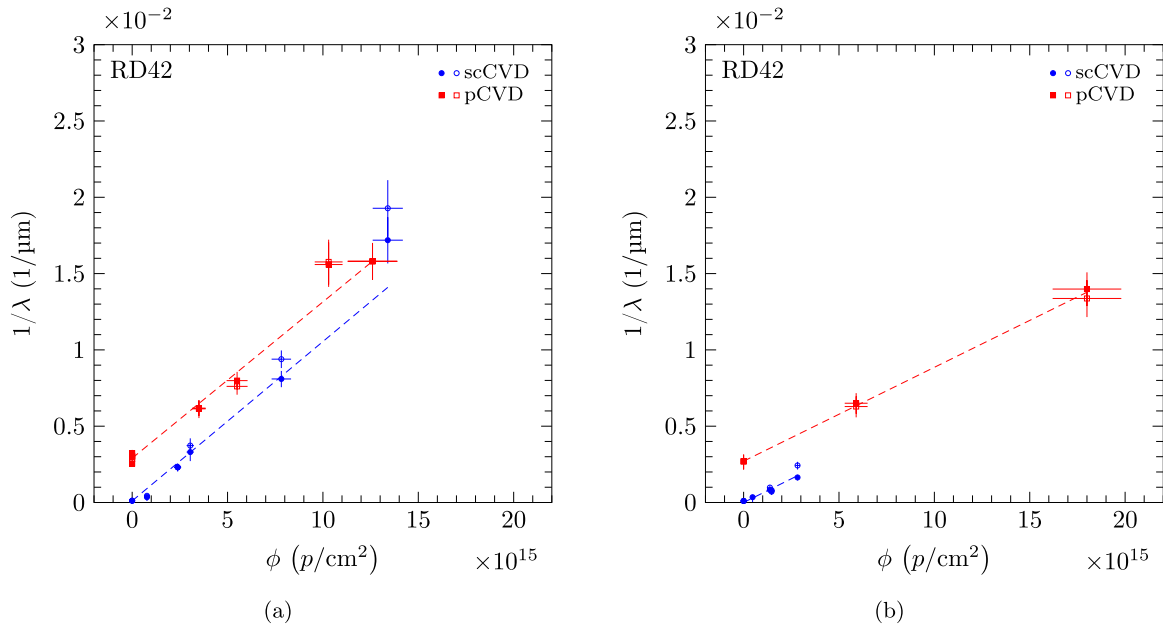
Figure 12. The $1/\lambda$ for each type of diamond in the (a) 800 MeV irradiation and (b) 24 GeV irradiation. The two values shown at each fluence are the values for positive (solid markers) and negative (open markers) bias at $E = 2$ V μm^{-1}. Each type was fit with an individual simple damage curve.
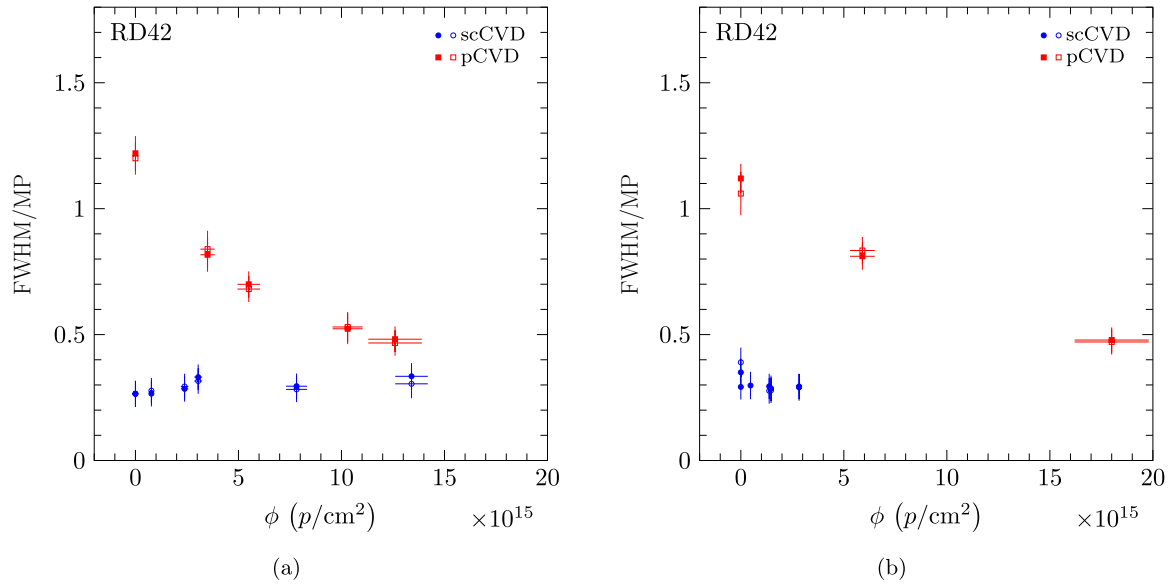

Figure 13. The FWHM/MP for each type of diamond in the (a) 800 MeV irradiation and (b) 24 GeV irradiation. The two values shown at each fluence are the values for positive (solid markers) and negative bias (open markers) at $E = 2$ V μm^{-1}.

Figure 10(b) shows the data and the linear fits for each of the 24 GeV irradiated samples.

In order to determine the consistency of the results for various samples and whether the data should be combined and fit, the damage constants of each individual sample for the 800 MeV irradiation are plotted in figure 11(a) and the individual damage constants for the 24 GeV irradiation are plotted in figure 11(b).

To obtain the effect of the *ccd* statistical and systematic uncertainties on the damage constant, the fit was performed twice considering first only statistical uncertainties of the *ccd* and second including the full set of statistical and systematic uncertainties. A small dependence of the signal on the polarity of the applied electric bias field was observed. Therefore, the fit was repeated using only runs of the same bias polarity. A difference of $^{+2.5\%}_{-2.6\%}$ ($^{+9.0\%}_{-6.3\%}$) in the damage constant of 800 MeV (24 GeV) protons was observed and added in quadrature to the systematic uncertainty. To estimate the systematic effect of the choice of the ratio λ_h/λ_e on the damage constant, the fit was repeated with the ratio λ_h/λ_e varied in a range from 0.7 to 2.1. The maximum observed difference in both directions of $^{+0.4\%}_{-2.5\%}$ ($^{+0.9\%}_{-6.2\%}$) in the damage constant of 800 MeV (24 GeV) protons was assigned as systematic uncertainty on the damage constant.
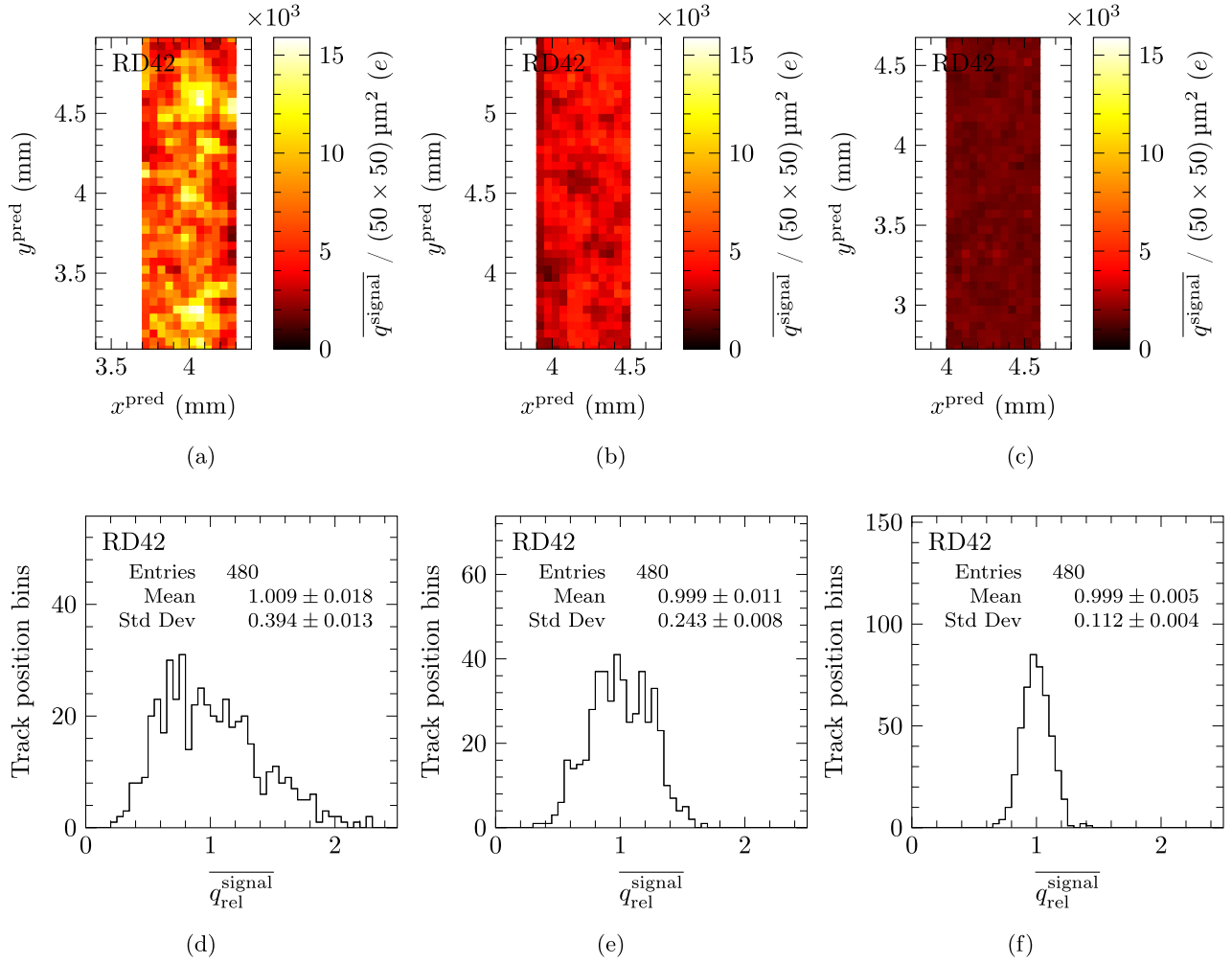
Figure 14. The mean signal charge in pCVD sample 5 as a function of *xy* position in 50×50 μm bins. The positions in the sample are the same for each figure shown although the position in tracking space has changed slightly for each beam test. The mean signal charge distribution of 50×50 μm track position bins of these distributions is shown in figures (d)–(f) normalized by the overall average. (a), (d) Before the 24 GeV irradiation (b), (e) after a fluence of 5.9×10^{15} 24 GeV p cm^{-2} and (c), (f) after a fluence of 18.0×10^{15} 24 GeV p cm^{-2}.

7. Measurement of damage coefficients

Due to the consistency of the damage coefficients for the individual samples, the data for each irradiation energy were combined by diamond type, i.e. pCVD or scCVD. In figure 12(a), we present the final fit results for the 800 MeV proton irradiation for pCVD and scCVD types of diamond. In figure 12(b), we present the final fit results for the 24 GeV proton irradiation for pCVD and scCVD types of diamond. The final results are:

$$k_{\text{scCVD}}^{800\ \text{MeV}} = 1.04\ ^{+0.03}_{-0.03}\ (\text{stat})\ ^{+0.06}_{-0.07}\ (\text{syst}) \times 10^{-18}\ \text{cm}^2\ (p\ \mu\text{m})^{-1}$$
$$k_{\text{pCVD}}^{800\ \text{MeV}} = 1.02\ ^{+0.04}_{-0.04}\ (\text{stat})\ ^{+0.05}_{-0.05}\ (\text{syst}) \times 10^{-18}\ \text{cm}^2\ (p\ \mu\text{m})^{-1}$$
$$k_{\text{scCVD}}^{24\ \text{GeV}} = 0.62\ ^{+0.01}_{-0.01}\ (\text{stat})\ ^{+0.10}_{-0.09}\ (\text{syst}) \times 10^{-18}\ \text{cm}^2\ (p\ \mu\text{m})^{-1}$$
$$k_{\text{pCVD}}^{24\ \text{GeV}} = 0.62\ ^{+0.03}_{-0.03}\ (\text{stat})\ ^{+0.05}_{-0.05}\ (\text{syst}) \times 10^{-18}\ \text{cm}^2\ (p\ \mu\text{m})^{-1}.$$

Since the final results by diamond type are in agreement indicating both CVD species follow the same radiation damage mechanism we quote the overall damage constant for diamond material as:

$$k_{\text{diamond}}^{800\ \text{MeV}} = 1.04\ ^{+0.02}_{-0.02}\ (\text{stat})\ ^{+0.04}_{-0.05}\ (\text{syst}) \times 10^{-18}\ \text{cm}^2\ (p\ \mu\text{m})^{-1}$$
$$k_{\text{diamond}}^{24\ \text{GeV}} = 0.62\ ^{+0.01}_{-0.01}\ (\text{stat})\ ^{+0.06}_{-0.06}\ (\text{syst}) \times 10^{-18}\ \text{cm}^2\ (p\ \mu\text{m})^{-1}.$$

8. Measurement of pulse height FWHM/MP

Figure 9 shows the evolution of the raw pulse height for a diamond as a function of fluence. For an unirradiated detector the resolution for measuring the energy of a particle is related to the full width at half maximum (FWHM) of the pulse height distribution measured in the material. The smaller the FWHM

J. Phys. D: Appl. Phys. **52** (2019) 465103

L Bäni *et al*

the better the measurement of the energy for a given number of events. In practice, the relative FWHM resolution, i.e. the FWHM normalized to the mean of the distribution, is used to compare the energy resolution of different materials. In our case, we have two potentially different materials (pCVD and scCVD diamond) and at each fluence the material may be different due to radiation damage of the material. To compare the two materials and multiple fluences we used the relative FWHM resolution normalizing each distribution to the most probable (MP) value of the distribution since the inherent energy loss distribution is 'Landau-like' and the mean of a Landau distribution depends on the number of events attained. Thus, our variable of interest, the relative FWHM resolution, R, is given by:

$$R = \frac{\text{FWHM}}{\text{MP}}. \tag{6}$$

We calculated the quantity R as a function of fluence for both the 800 MeV irradiation data and the 24 GeV irradiation data. In all of the data taken, the particles used to measure the energy loss were $+120$ GeV hadrons. The measured signal charge is composed of the energy loss distribution convoluted with the electronic noise distribution. In order to extract the inherent energy loss distribution we deconvoluted the electronic noise from the measured signal charge distribution. To perform the deconvolution, we used the measured CMC noise for each channel and constructed the distribution for five strips by convoluting five individual strip noise distributions. Further we required the convoluted noise distribution generated in this way reflect the actual hit distribution among strips. Using the deconvoluted signal charge as a function of fluence for each sample we computed the quantity R.

In figure 13(a), we present the 800 MeV irradiation results and in figure 13(b) we present the 24 GeV irradiation results. For both irradiation energies, R decreases for pCVD samples as a function of fluence. The slopes of the pCVD curves are different in figures 13(a) and (b) indicating the slope may depend on the initial quality of the sample and/or irradiation source. For the scCVD samples, R is consistent (i.e. within statistical errors) with being flat as a function of fluence. Moreover, the results for R for the scCVD samples irradiated at 24 GeV up to a fluence of 3×10^{15} p cm^{-2} are consistent with the results from the 800 MeV irradiation up to the same fluence.

9. Measurement of uniformity

The initial non-uniformities in unirradiated pCVD material are mainly due to the interior crystal structure where single grains have different charge collection properties causing a spatial dependence of the Landau-like distributions in the material. This feature is clearly indicated in figure 14(a) which shows the mean signal charge as a function of xy position in the sample in 50×50 μm bins for the unirradiated sample 5. All other pCVD samples have similar distributions. In figures 14(b) and (c), we show the same xy region in sample 5 after 5.9×10^{15} 24 GeV p cm^{-2} and 18.0×10^{15} 24 GeV p cm^{-2}

respectively. As the sample is irradiated, not only does the mean charge decrease according to (4) but also the spread in the mean charge decreases. This is also a consequence of (4), which can be seen by rewriting (4) as

$$\lambda = \frac{\lambda_0}{1 + \lambda_0 k \phi} \tag{7}$$

and upon taking the derivative, $d\lambda/d\phi$, we find:

$$\frac{d\lambda}{d\phi} = -k\lambda^2. \tag{8}$$

Simply stated, equation (8) predicts for a non-uniform material the portions of the material with the largest λ are damaged most for a given fluence increase, $d\phi$. Equation (8) also indicates samples with the largest k are damaged most for a given fluence increase, $d\phi$.

In figures 14(d)–(f), the distributions of the relative average pulse height measured in the 50×50 μm xy position bins of figures 14(a)–(c) is shown. The standard deviations of the distributions are observed to decrease as a function of fluence by nearly a factor of four indicating the relative variations in normalized pulse height across the material are decreasing as a function of fluence. Before irradiation the standard deviation of the normalized pulse height in sample 5 was 0.394 and after a 24 GeV proton fluence of 18.0×10^{15} p cm^{-2} the distribution is observed to be much narrower with a standard deviation of 0.112. Figure 14 indicates that the non-uniformities in pCVD material decrease with irradiation fluence. Since unirradiated scCVD material is essentially uniform with a standard deviation of the normalized pulse height across the material of 0.064 we expect no change in the standard deviation as a function of fluence. We observe after an 800 MeV proton fluence of 13.4×10^{15} p cm^{-2} the distribution has a standard deviation of 0.080.

The quantity R which is a measure of the normalized energy resolution is then related to the 'uniformity' of the material. The smaller the quantity R the narrower the normalized pulse height distribution is across the material. Figures 13 and 14 taken together indicate that pCVD material becomes more uniform with fluence for both 800 MeV and 24 GeV irradiations and the uniformity of scCVD material is independent of fluence for both 800 MeV and 24 GeV irradiations.

10. Summary

In this article, we present the results of our studies of pCVD and scCVD diamond material both before and after a series of proton irradiations with 800 MeV and 24 GeV particles. Our results indicate the decrease in signal charge in both pCVD and scCVD material follows a simple damage model. Moreover, for a given irradiation energy our results indicate both pCVD and scCVD diamond material have the same damage constant. Our measurements of the damage constants in CVD diamond presented in this article are the most precise to date. From the evolution of the signal charge distributions as a function of fluence our results indicate the FWHM/MP for pCVD diamond material decreases with fluence while the

J. Phys. D: Appl. Phys. **52** (2019) 465103

L Bäni *et al*

FWHM/MP of scCVD material is flat with fluence. Finally, from the *xy* position distribution of the normalized pulse height pCVD material becomes more uniform with fluence and scCVD material stays constant.

Acknowledgments

ORCID iDs

L Bäni https://orcid.org/0000-0001-9966-8788
F Bachmair https://orcid.org/0000-0001-5670-3184
C Dorfer https://orcid.org/0000-0002-2163-442X
A Gorišek https://orcid.org/0000-0002-3903-3438
D Hits https://orcid.org/0000-0002-3135-6427
A Lacoste https://orcid.org/0000-0002-4268-6288
G Kramberger https://orcid.org/0000-0002-7580-384X
M Mikuž https://orcid.org/0000-0002-4119-6156
A Oh https://orcid.org/0000-0001-9025-0422
R Perrino https://orcid.org/0000-0002-5764-7337
R Wallny https://orcid.org/0000-0001-8038-1613

References

[1] CERN The European Organization for Nuclear Research, CH-1211, Genève 23, (https://home.cern/)
[2] Mauro De Palma D *et al* 2002 Development of radiation hard semiconductor: devices for very high luminosity colliders *R&D Proposal* LHCC 2002-003 P6
[3] Apollinari G *et al* 2015 High-luminosity Large Hadron Collider (HL-LHC): preliminary design report *CERN Yellow Reports: Monographs* CERT-2015-005 (Geneva: Cern) (https://doi.org/10.5170/CERN-2015-005.1)
[4] Apollinari G *et al* 2017 High-luminosity Large Hadron Collider (HL-LHC): technical design report *CERN Yellow Reports: Monographs* vol 4/2017 CERN 2017-007-M (Geneva: CERN) (https://doi.org/10.23731/CYRM-2017-004)
[5] Prins J F, Derry T E and Sellschop J P F 1986 Volume expansion of diamond during ion implantation *Phys. Rev.* B **34** 8870
[6] Koike J, Parkin D M and Mitchell T E 1992 Displacement threshold energy for type IIa diamond *Appl. Phys. Lett.* **60** 1450
[7] Nazaré M H *et al* (RD42 Collaboration) 1994 Development of diamond tracking detectors for high-luminosity experiments at the LHC *Report* Proposal/RD42 CERN/DRDC 94-21/P56
[8] Artuso M *et al* (RD42 Collaboration) 2017 RD42 status report: development of diamond tracking detectors for high-luminosity experiments at the LHC *Report* CERN-LHCC-2017-006
[9] Kagan H *et al* (RD42 Collaboration) 2018 RD42 status report: development of diamond tracking detectors for high-luminosity experiments at the LHC and beyond *Report* CERN-LHCC-2018-015; LHCC-SR-005
[10] Pernegger H *et al* 2005 Charge-carrier properties in synthetic single-crystal diamond measured with the transient-current technique *J. Appl. Phys.* **97** 073704
[11] deBoer W *et al* 2007 Radiation hardness of diamond and silicon sensors compared *Phys. Status Solidi* a **204** 3004
[12] Tsung J-W *et al* 2012 Signal and noise of diamond pixel detectors at high radiation fluences *J. Instrum.* **7** P09009
[13] Re V *et al* (BaBar Collaboration) 2004 Radiation hardness and monitoring of the BaBar vertex tracker *Nucl. Instrum. Methods* A **518** 290
[14] Edwards A *et al* (BaBar Collaboration) 2004 Radiation monitoring with diamond sensors in BaBar *IEEE Trans. Nucl. Sci.* **51** 1808
[15] Edwards A *et al* (BaBar Collaboration) 2005 Radiation monitoring with CVD diamonds in BaBar *Nucl. Instrum. Methods* A **552** 176
[16] Eusebi R *et al* (CDF Collaboration) 2006 A diamond based beam condition monitor for the CDF experiment *IEEE Nuclear Science Symp. Conf. Record N18-2* p 709
[17] Dong P *et al* (CDF Collaboration) 2008 Beam condition monitoring with diamonds at CDF *IEEE Trans. Nucl. Sci.* **55** 328
[18] Gorisek A *et al* (ATLAS Collaboration) 2007 ATLAS diamond beam condition monitor *Nucl. Instrum. Methods* A **572** 67
[19] Cindro V *et al* (ATLAS Collaboration) 2008 The ATLAS beam conditions monitor *J. Instrum.* **3** 02004
[20] Bell A *et al* (CMS Collaboration) 2008 Beam and radiation monitoring for CMS *IEEE Nuclear Science Symp. Conf. Record N30-242* p 2322
[21] Bartz E *et al* (CMS Collaboration) 2009 The PLT: a luminosity monitor for CMS based on single-crystal diamond pixel sensors *Nucl. Phys.* B **197** 171
[22] Domke M *et al* (LHCb Collaboration) 2008 Commissioning of the beam conditions monitor of the LHCb experiment at CERN *IEEE Nuclear Science Symp. Conf. Record N58-6* p 3306
[23] Zhao S 1994 Characterization of the electrical properties of polycrystalline diamond films *PhD Dissertation* Ohio State University
[24] Landau L D 1944 On the energy loss of fast particles by ionization *J. Phys. USSR* **8** 201
[25] Vavilov P V 1957 Ionization losses of high-energy heavy particles *Sov. Phys.—JETP* **5** 749
[26] Bichsel H 1988 Straggling in thin silicon detectors *Rev. Mod. Phys.* **60** 663
[27] Tanabashi M *et al* (Particle Data Group) 2018 Review of particle physics *Phys. Rev.* D **98** 030001
[28] Dotite silver paint D-550. Fujikura Kasei Co., LTD. 6-15, Shibakoen 2-chome, Minato-ku, Tokyo 105-0011 Japan; TEL. 81-3-3436-1100 (https://www.fkkasei.co.jp/english/product/electric/dotite/05.html)
[29] Integrated Detector and Electronics (IDE) AS designed the VA circuits www.ideas.no

J. Phys. D: Appl. Phys. **52** (2019) 465103

L Bäni *et al*

[30] Colledani C *et al* 1996 A submicron precision silicon telescope for beam test purposes *Nucl. Instrum. Methods* A **372** 379

[31] Palni P 2014 Evidence for the heavy Baryon resonance state Λ_b^{*0} observed with the CDF II detector, and studies of new particle tracking technologies using the LANSCE proton beam *PhD Thesis* The University of New Mexico

[32] Adam W *et al* (RD42 Collaboration) 2006 Radiation hard diamond sensors for future tracking applications *Nucl. Instrum. Methods* A **565** 278

[33] Velthuis J J *et al* (RD42 Collaboration) 2008 Radiation hard diamond pixel detectors *Nucl. Instrum. Methods* A **591** 221

[34] Bachmair F 2016 CVD diamond sensors in detectors for high energy physics *PhD Thesis* ETH Zurich

[35] Bäni L 2017 Top quarks and diamonds *PhD Thesis* ETH Zurich

[36] The VA2 Specifications, Integrated Detector and Electronics AS (https://cds.cern.ch/record/2687447)

[37] Hartjes F *et al* (RD42 Collaboration) 1999 Parameterisation of radiation effects on CVD diamond for proton irradiation *Nucl. Phys.* B **78** 675

[38] Schockley W 1938 Currents to conductors induced by a moving point charge *J. Appl. Phys.* **9** 635

[39] Ramo S 1939 Currents induced by electron motion *Proc. IRE* **27** 584

[40] Hecht K 1932 Zum Mechanismus des lichtelektrischen Primärstromes in isolierenden Kristallen *Z. Phys.* **77** 235

[41] Kölbig K S 1985 Landau distribution, CERNLIB-G110 (http://cds.cern.ch/record/2050932)